Toward Ultimate Nanoplasmonics Modeling

Diego M. Solís,[†] José M. Taboada,[‡] Fernando Obelleiro,[†,*] Luis M. Liz-Marzán,[§,⊥] and F. Javier García de Abajo[∥,¶,*]

[†]Departamento de Teoría de la Señal y Comunicaciones, University of Vigo, 36301 Vigo, Spain, [‡]Departamento de Tecnología de los Computadores y de las Comunicaciones, University of Extremadura, 10003 Cáceres, Spain, [§]Bionanoplasmonics Laboratory, CIC biomaGUNE, 20009 Donostia - San Sebastian, Spain, [⊥]Ikerbasque, Basque Foundation for Science, 48011 Bilbao, Spain, [∥]ICFO—The Institute of Photonic Sciences, Mediterranean Technology Park, 08860 Castelldefels (Barcelona), Spain, and [¶]ICREA—Institució Catalana de Reserca i Estudis Avançats, Passeig Lluís Companys 23, 08010 Barcelona, Spain

ABSTRACT Advances in the field of nanoplasmonics are hindered by the limited capabilities of simulation tools in dealing with realistic systems comprising regions that extend over many light wavelengths. We show that the optical response of unprecedentedly large systems can be accurately calculated by using a combination of surface integral equation (SIE) method of moments (MoM) formulation and an expansion of the electromagnetic fields in a suitable set of spatial wave functions *via* fast multipole methods. We start with a critical review of volume *versus* surface integral methods, followed by a short tutorial on the key features that render plasmons useful for sensing (field enhancement and confinement). We then use the SIE-MoM to examine the plasmonic and sensing capabilities of various systems with increasing degrees of complexity, including both individual and interacting gold nanorods and nanostars, as well as large random and periodic arrangements of ~1000 gold nanorods. We believe that the present results and methodology raise the standard of numerical electromagnetic simulations in the field of nanoplasmonics to a new level, which can be beneficial for the design of advanced nanophotonic devices and optical sensing structures.

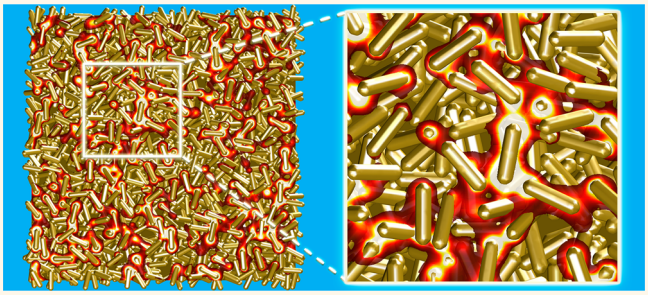

Recent advances in nanotechnology, combined with the prospect of a plethora of applications ranging from biosensing to optical signal processing, have stimulated a large interest in the field of plasmonics, which exploits the subwavelength confinement, enhancement, and spatiotemporal control of light at metal/dielectric interfaces and, in particular, in metallic nanoparticles.[1,2] The rise of plasmonics has materialized in cutting-edge applications to medicine (*e.g.*, cancer therapy[3]), nanoscale light management,[4] deep-subwavelength optical microscopy and lithography,[5] enhanced photovoltaics,[6] nanolasing,[7] and quantum optics.[8]

The metallic optical response underlying the existence of plasmons is dominated by polarization and excitation of valence electrons, which can be regarded as a plasma capable of sustaining collective oscillations. The quanta of these oscillations are known as plasmons, and their frequency increases with the electron density. Although a quantum-mechanical treatment is required to understand the statistics and true physical nature of these excitations,[9] as well as the rules governing their interactions with elementary probes,[10] the optical response of plasmonic metals is generally well-described by classical electrodynamics relying on the use of local, frequency-dependent dielectric functions.[11] Remarkably, such a classical approach produces predictive results for particle and surface feature sizes down to ~1 nm, a distance below which nonlocal effects become significant.[12,13] The theoretical understanding of plasmons and the design of plasmonic nanostructures can therefore directly benefit from knowledge gathered in electrical engineering, antenna design, and other classical areas in which the solution of the electromagnetic problem plays a central role.

Importantly, plasmons imprint a characteristic resonant behavior on the dielectric function, which acquires a large negative real part.[14] In an intuitive picture, the conduction

* Address correspondence to obi@com.uvigo.es, javier.garciadeabajo@icfo.es.

Published online July 31, 2014
10.1021/nn5037703

electrons of an irradiated nanoparticle react toward the externally applied electric field, producing a net charge displacement from the equilibrium position and subsequently experiencing the restoring force of the remaining positive ionic background. This leads to plasmon collective oscillations of natural frequencies lying in the visible and near-infrared (vis–NIR) parts of the spectrum, although their precise position is strongly dependent on particle morphology, composition, and environment.[15]

When the structures are small compared with the illumination wavelength, their response is scale-invariant, so that the resulting plasmons are determined by geometry and dielectric function rather than the actual sizes of the particles.[16] Deep-subwavelength plasmons are thus observed, as we argue below for the instructive example of two closely spaced spheres in a dimer. Larger structures involve retardation and require solving Maxwell's equations, which yield analytical solutions only for highly symmetric geometries (*e.g.*, the sphere[17]). In general, the study of the optical response of most nanometallic structures that we encounter in practice requires numerically intensive simulation tools. In this respect, there are several popular methods that are capable of yielding rigorous classical electromagnetic solutions in arbitrary geometries. In particular, volume approaches such as the discrete-dipole approximation (DDA),[18] the finite-difference in the time domain (FDTD),[19] and frequency-domain finite-element methods (FEMs)[20,21] benefit from relatively simple parametrizations, typically consisting of filling the three-dimensional (3D) space with a representative set of elements, in which either the electromagnetic fields or the local polarizations are self-consistently calculated. This requires solving a linear set of equations with a resulting numerical demand that scales with at least the square of the volume. Although these approaches are increasingly popular, partly due to the availability of commercial software (*e.g.*, COMSOL), they cannot cope with structures spanning several wavelengths in size, as the required computational demand becomes impractical using reasonable computer power capabilities.

In this Perspective, we combine a Galerkin's method of moments formulation with the most recent advances in spectral acceleration techniques for the simulation of realistic large-scale plasmonic systems.

A more computationally efficient approach comprises the use of a surface integral equation (SIE) formulation, which has been successfully combined with an *ad hoc* suitable implementation of the method of moments (MoM).[22,23] Although not yet widespread in optics, these methods bring important advantages when compared to the above-mentioned volumetric approaches. Namely, they only require a parametrization of the two-dimensional (2D) interfaces involved, rather than a 3D space embedding of the material structure, thus resulting in a considerable reduction in the number of unknowns. Furthermore, no absorbing boundary conditions or surrounding empty space need to be specifically parametrized. Additionally, these methods are less sensitive to instabilities produced by rapid spatial variations of the permittivity, as is usually the case in plasmonic structures. A point representation formulation of the SIE boundary-element method (BEM) has been successfully used to explain the optical response of a vast number of nanostructured morphologies characterized by different techniques ranging from optical spectroscopy[15] to electron energy loss spectroscopy[24] and cathodoluminescence.[25]

In this Perspective, we combine Galerkin's method of moments formulation with the most recent advances in spectral acceleration techniques, based on the multilevel fast multipole algorithm (MLFMA)[26] and the fast Fourier transform (FFT), for the simulation of realistic large-scale plasmonic systems. The presented solver (called M^3, the newest version of the former HEMCUVE[27,28]) has previously been applied to plasmonics for the solution of problems such as the design of nanoantennas[29,30] and optical wireless nanolinks.[31] We illustrate the great potential of this approach by presenting a number of simulations for various nanostructures with increasing degrees of complexity. We outline below the main elements of the method, but we first discuss, in a tutorial manner, two important properties of plasmons—light confinement and enhancement—that enable most of the applications noted above.

Plasmon Confinement and Field Enhancement. Spatial confinement and field enhancement are two of the main properties of localized plasmons, enabling them to be used for optical sensing down to single-molecule sensitivity. Plasmons can be localized in the so-called hotspots of a metallic nanostructure, the sizes of which are generally small compared with the wavelength of the light used to excite them. We can thus gain insight into their optical properties by neglecting retardation effects and analyzing them in the electrostatic limit. This is precisely what we do in Figure 1 for a prototypical plasmonic structure consisting of a pair of closely spaced metallic spheres. As shown in Figure 1a, the dimer acts as a comparatively large object capable of sustaining a dipole $\mathbf{p}$ in response to the incident-light electric field $\mathbf{E}^{inc}$. The magnitude of this dipole is

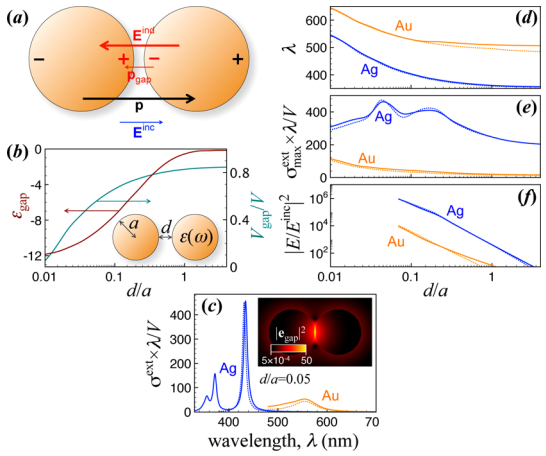

Figure 1. Field confinement and enhancement of a localized plasmon. (a) Characteristic structure supporting gap plasmons and consisting of two spheres separated by a narrow gap. This system illustrates how charge neutrality within each of the spheres contributes to produce large field enhancement. (b) Resonant real value of the spheres' permittivity (left) at which the gap plasmon appears, as a function of the gap-to-radius ratio *d*/*a* (see inset). The right scale shows the weight of the gap plasmon in the extinction spectra. (c) Normalized extinction spectra of silver and gold dimers of the same dimensions. (d–f) Gap plasmon resonant wavelength (d), extinction maximum (e), and electric field intensity enhancement (f). The dielectric functions of silver and gold are taken from tabulated optical measurements.[33] Full electromagnetic simulations for a sphere radius *a* = 10 nm (solid curves) are compared with analytical electrostatic theory (dotted curves) in (c–f).

enhanced when the light frequency is in resonance with the gap plasmon, but most importantly, due to charge neutrality, each of the spheres contributes with a charge of opposite sign near the gap region, thus producing an additional small dipole $\mathbf{p}_{gap}$ (because these charges are separated by a small gap distance d) and a high induced field $\sim 1/d$ (because the gap forms a capacitor of narrowly spaced *plates*). Consequently, we can trace the origin of field confinement and enhancement back to the combined effect of (i) charge neutrality in each of the spheres and (ii) the capacitor of closely spaced *plates* formed in narrow gaps.[32]

The dimer gap mode shows up as the longest wavelength feature in the extinction spectra shown in Figure 1c, which also illustrates a blue shift of the silver plasmon relative to gold as a result of weaker d-band screening (both metals have similar s-band electron density, but screening by deeper bands shifts the plasmon down in frequency). Moreover, the lower level of inelastic optical losses in silver compared with that in gold leads to narrower features that allow us to resolve higher-order plasmons emerging at shorter wavelengths.[34] A near-field map at the gap plasmon frequency (see inset to Figure 1c) reveals the strong degree of confinement to the gap region. The light wavelength of this mode, its contribution to the extinction cross section, and its associated maximum near-field intensity enhancement at the gap center are analyzed in Figure 1d–f as a function of the ratio between gap distance and sphere radius, d/a. A general increase of all of these magnitudes with decreasing gap distance is observed, and, in particular, the intensity enhancement reaches extremely large values $>10^5$ with combinations of gap and sphere sizes for which the local dielectric theory under consideration is still applicable (narrower gaps involve nonlocal effects beyond the scope of this work[12]). Such large near-field amplification is required to achieve the reported $>10^{10}$ surface-enhanced Raman scattering (SERS) enhancement in controlled hotspots.[35,36]

The numerical results shown in Figure 1c–f for the simple dimer system (solid curves) can be well approximated using fully analytical formulas (dotted curves) based upon an eigenmode analysis of Poisson's equation. Indeed, the self-consistent field admits an expansion in terms of eigenmodes of the system,[16] based upon which we can rigorously write the polarizability as

$$\alpha(\omega) = \frac{1}{4\pi}\sum_j V_j g_j(\omega) \qquad (1)$$

and the induced electric field as

$$\mathbf{E}^{ind}(\mathbf{r},\omega) = \sum_j \mathbf{e}_j(\mathbf{r}) g_j(\omega) \qquad (2)$$

(assuming an overall $\exp(-i\omega t)$ time dependence), where we have defined the spectral functions

$$g_j(\omega) = \left[\frac{1}{\varepsilon(\omega)-1} - \frac{1}{\varepsilon_j - 1}\right]^{-1}$$

while the sums run over eigenmodes j of (real, negative) resonant permittivity ε_j and associated electric field $\mathbf{e}_j(\mathbf{r})$. Equations 1 and 2 can be readily applied to any choice of material by plugging the corresponding dielectric function $\varepsilon(\omega)$ into $g_j(\omega)$. In the $\varepsilon \to 1$ limit, a perturbative expansion shows that the partial volumes V_j implicitly defined in eq 1 add up to the total volume V occupied by the material (*i.e.*, $\Sigma_j V_j = V$, where $V = 8\pi a^3/3$ for a dimer). Now, for frequencies near a dominant, spectrally isolated plasmon, it is enough to use a single coefficient in the above sums. In particular, we present in Figure 1b the values of ε_j and V_j for the dimer gap mode. This allows us to retrieve the light wavelength corresponding to this plasmon directly by solving the equation $\mathrm{Re}\{\varepsilon\} = \varepsilon_j$ (Figure 1d, dotted curve), as well as the maximum extinction cross section (Figure 1e)

$$\sigma^{ext}_{max} \approx 2\pi \frac{(\varepsilon_j - 1)^2}{\mathrm{Im}\{\varepsilon\}} \frac{V_j}{\lambda}$$

and the field enhancement (Figure 1f)

$$|E/E^{inc}|^2 \approx |\mathbf{e}_j(\mathbf{r})|^2 \left|\frac{(\varepsilon_j - 1(\varepsilon - 1)}{\mathrm{Im}\{\varepsilon\}}\right|^2 \qquad (3)$$

The agreement between these analytical formulas (Figure 1c–f, dotted curves) and full numerical simulations

(solid curves) is remarkably good for the selected mode. Incidentally, the density plot of Figure 1c shows precisely $|\mathbf{e}_j(\mathbf{r})|^2$ for $d/a = 0.05$, and, thus, it defines the near-field profile of the gap plasmon *via* eq 3, which is independent of the choice of material, provided the plasmon mode is spectrally isolated.

The electrostatic dimer provides a tutorial approach into localized plasmons, which is only quantitatively relevant for small particle sizes. Unfortunately, commonly exploited nanostructures involve more complex geometries and larger dimensions that produce strong retardation effects. Next, we describe what we believe is an extraordinarily efficient suite of methods to simulate their optical response, and we discuss several examples of their application.

Multilevel Fast Multipole Algorithm Solver. Based on Love's equivalence principle,[37] metallic nanostructures can be replaced by equivalent electric and magnetic currents distributed over the boundary surfaces and interfaces. The total electromagnetic fields can be obtained as a superposition of the known incident fields and the unknown scattered fields, which can be self-consistently obtained from the equivalent currents through the integro-differential Stratton–Chu representation formulas[38,39] and the 3D electrodynamic homogeneous Green's function. More precisely, we derive a set of SIEs for the unknown equivalent currents by imposing the well-known continuity of the tangential fields at the boundaries. These SIEs are subsequently discretized by applying the Galerkin MoM procedure[22] using a set of known basis and testing functions, leading to a dense matrix system of linear equations. This results in a linear system of N equations and N unknowns—the number of basis functions used to expand the currents. As noted above, this method, which we term SIE-MoM, brings about important advantages with respect to volumetric approaches, namely, a relatively reduced numerical size (2D *vs* 3D) and greater stability, particularly when dealing with resonant metallic response.

In order to extend the practical applicability of the SIE method to even larger structures, considerable effort has been made toward the development of fast, efficient algorithms that can reduce the elevated costs of the traditional MoM ($O(N^3)$ with direct inversion of the dense matrix system and $O(N^2)$ using iterative solvers), in terms of both storage and computer processing time. Specifically, we single out the fast multipole method (FMM)[40] and its variants, the multilevel fast multipole algorithm (MLFMA),[26] and the MLFMA combined with the fast Fourier transform.[27] Based on Gegenbauer's addition theorem for the homogeneous Green function, the FMM reduces the computational cost to $O(N^{3/2})$, whereas its multilevel version achieves $O(N \log N)$ by incorporating plain and adjoint interpolation schemes for the fields. The FFT extension of the latter (MLFMA-FFT) combines the algorithmic efficiency of MLFMA with high scalability *via* parallelization using multicore computer clusters. As an indication of its power, the MLFMA-FFT method has recently been used to solve an electromagnetic problem with 1 billion unknowns,[27] which, to our knowledge, is the largest MoM-solved problem to date. The interested reader can find more details about this formulation in the Supporting Information (SI).

As an indication of its power, the MLFMA-FFT method has recently been used to solve an electromagnetic problem with 1 billion unknowns.

RESULTS AND DISCUSSION

With the aim of illustrating the great potential of the SIE-MoM method for plasmonics, we solve a number of currently relevant problems, in increasing order of complexity, showing its high versatility and computational power.

Gold Nanorods. Among the wide variety of existing nanoplasmonic systems, gold nanorods provide a reference platform for many practical applications. The currently available high degree of synthetic control, through both lithographic and wet chemistry methods, enables the accurate tailoring of the (longitudinal) plasmon resonances of gold nanorods through simple variations of their aspect ratio. In addition, the tunable anisotropy of these nanoparticles provides a plethora of opportunities for coupling plasmon modes in different manners. We have selected here a few simple examples of how the SIE-MoM can be applied to predict the optical responses of isolated and coupled nanorods accurately.

As a paradigmatic system, the extinction spectra of gold nanorods have been calculated in many different ways. In the long-wavelength limit, the Mie-Gans analytical formulation for prolate ellipsoids yields reasonable agreement with measured data taken from small particles compared with the illumination wavelength.[41] Inclusion of both retardation for larger particles and the actual nanorod shape, which deviates considerably from an ellipsoid, requires the use of fully numerical methods (*e.g.*, DDA, FDTD, or BEM), whose computational demand has prompted the use of approximate geometrical models, such as spherically capped cylinders. However, the actual nanorod morphology involves surface facets, which have been identified with high accuracy. In particular, a common class of rods appears as octagonal prisms capped by faceted tips.[42] Given the high versatility and accuracy of SIE-MoM, the experimentally determined nanorods' morphology and

dimensions can be readily implemented, assisted by a surface parametrization tool (SolidWorks software), with a rounding radius of 5 nm for tips and edges, as commonly observed in experiments.[42] Since plasmon resonances are highly dependent on particle morphology, in particular, for anisotropic shapes, the ensemble optical spectra measured from gold nanorod colloids unavoidably display inhomogeneous broadening, corresponding to an average over all illuminated nanorods, which feature slightly different dimensions, aspect ratios, and orientations. In accurate theoretical studies, this has been accounted for by obtaining a statistical distribution of dimensions, typically based on transmission electron microscopy (TEM) images, and then calculating extinction spectra for each population and weighing according to their relative abundances. This is illustrated in Figure 2a (crosses) for three different average aspect ratios, which reproduce recently reported experimental data.[43] Alternatively, the large computational capability of SIE-MoM, expedited *via* MLFMA, enables us to go one step further and to simulate a large number of nanorods with random positions and orientations (see inset in Figure 2a), displaying geometrical features (including polydispersity) accurately defined by the experimental data, and subsequently calculate the interaction of light with the whole ensemble in a single computational run (Figure 2a, dashed spectra). It can readily be seen that both calculations can reproduce the experimental data well. We can also use the SIE-MoM method to explore near-field properties, as illustrated in Figure 2b,c for the longitudinal and transverse plasmons of single gold nanorods with average dimensions corresponding to the samples simulated in Figure 2a. These electric near-field enhancement maps illustrate that the surface charges associated with the longitudinal plasmon modes are localized near the rod ends. Interestingly, the boundary currents used in the SIE-MoM method provide additional information of interest: regions of high electric current involve larger heating *via* inelastic losses, and these regions are generally different from the hotspots in which the induced charge and the fields reach high values (*i.e.*, hotspots involve high currents in adjacent regions, which are needed to supply and to evacuate the pileup of induced charge rapidly). This effect is observed in Figure 2b, where the surface electric currents exhibit a sinusoidal distribution that is consistent with the excitation of a half-wavelength antenna dipole (*i.e.*, a maximum at the rod center). Note that the effective wavelength is pinned by the rod size and corresponds to roughly twice the rod length.[44]

An example of plasmon coupling as described above is provided in Figure 2d,e for a nanorod dimer in tip-to-tip parallel configuration. Plasmon coupling leads to mode energy splitting, with strong dipole modes shifted down in energy and containing hotspots (see discussion of Figure 1 above). Apart from plasmon red shift and larger enhancement with decreasing gap separation, the surface current distributions now reveal convergence toward the gap hotspot, where charge accumulation and the capacitor effect lead to intensity enhancements up to 10^5.

Interestingly, a chiral arrangement of nanorods can produce optical chirality,[45] which is of current interest for potential applications in the analysis of different molecular enantiomers.[46] A simple example is shown in Figure 2f,g for two identical nanorods in a perpendicular orientation. When the rods lie in the same plane, no chirality is observed, but a strong chiral signal is predicted when introducing a vertical offset (Figure 2f). Figure 2h,i illustrates a more complex arrangement mimicking recent experiments[47] and also leading to large chirality.

Gold Nanostars. The high density of hotspots in nanostars suggests their application as excellent platforms for plasmon-assisted sensing[35,48] and photothermal therapy.[49] We illustrate the application of our methods to simulate nanostars and, for simplicity, concentrate on a symmetric structure containing 12 sharp tips branching out from a central spherical core (Figure 3). In particular, Figure 3a shows that longer tips produce more red-shifted plasmons, although the maximum value of absorption/scattering cross section is not very sensitive to this parameter. Near-field maps at the extinction maxima (Figure 3a, insets) neatly illustrate the enhancement at the tips, which increases for those that are oriented along the direction of the incident light polarization. Maximum currents near (but not at) the tips are also consistent with the picture drawn above from nanorods (see current maps in the insets to Figure 3a).

The decay rate of a point emitter is also known to suffer a large enhancement due to the interaction with localized plasmons. This effect is analyzed in Figure 3b,c for a molecule or quantum dot placed in the vicinity of a nanostar tip. The nonradiative and radiative components of the decay rate are computed from the self-induced near-field and the emitted far-field upon excitation with a point dipole oriented as shown in the figures.[50]

Plasmon coupling can also occur when nanostars approach each other, as described above for nanorods. In nanostars, however, the number of configurations leading to exceptionally efficient hotspots may increase due to their involved morphology. Examples are shown here for plasmon coupling and hotspot formation when two nanostar tips approach each other (Figure 3d,g), when a tip approaches a valley between three adjacent branches (Figure 3e,h), and when a tip approaches a valley between two adjacent branches lying in the same plane as the approaching branch (coplanar tip-to-valley configuration).

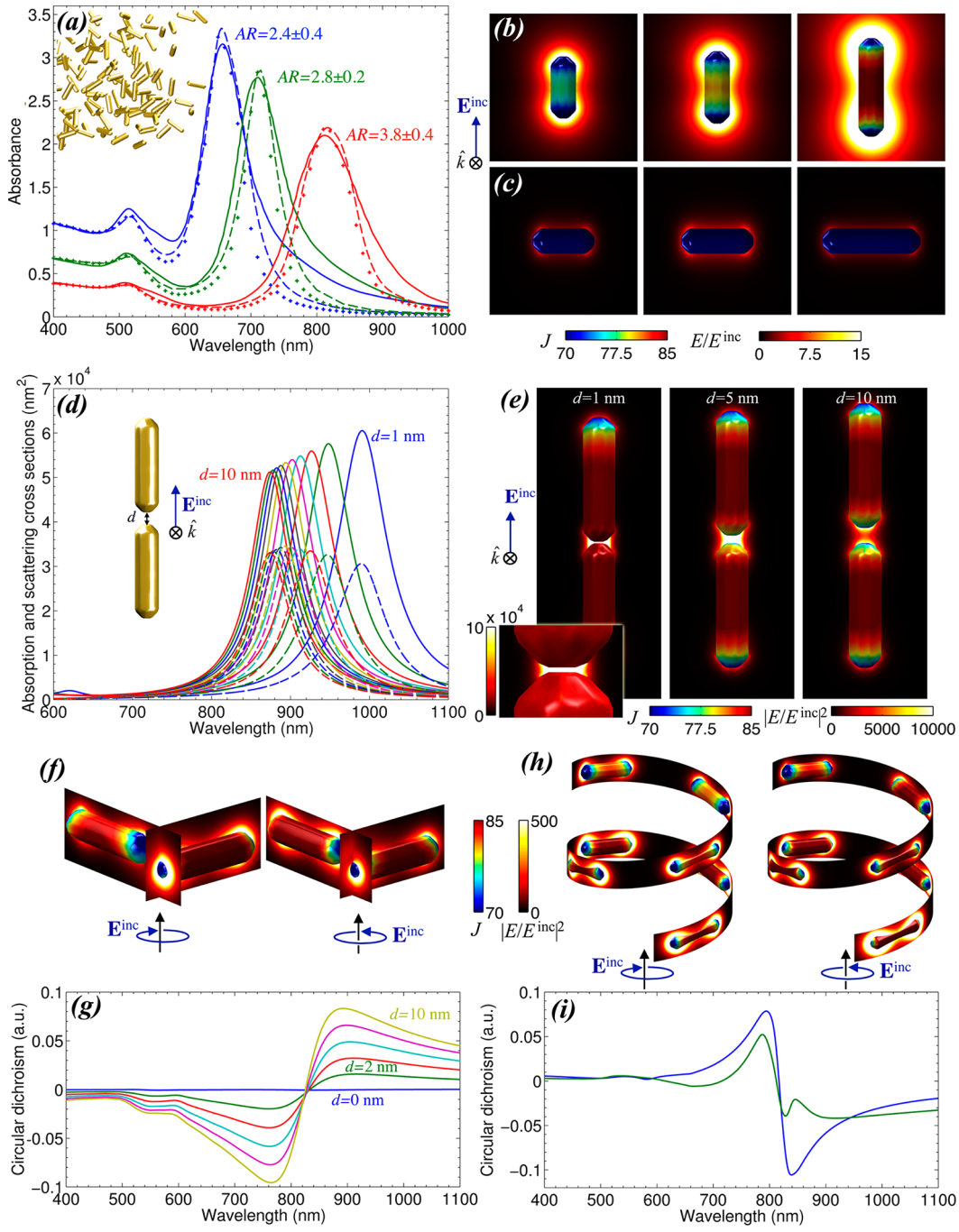

Figure 2. Modeling gold nanorods (GNRs). (a) Extinction spectra of water-dispersed GNRs with aspect ratios of 2.4, 2.8, and 3.8. Solid curves are measured spectra from ref 43. Copyright 2013 American Chemical Society. Dotted curves are calculations averaged over light incidence and polarization; dashed curves are calculations for samples consisting of 700 randomly oriented/positioned GNRs (average density is 1 GNR per 0.08 μm^3). The inset shows an example of nanorod distribution (not at scale). (b,c) Calculated near-field enhancement maps and surface current distributions for the longitudinal (b) and transverse (c) plasmons of the same rods as in (a). (d,e) Extinction spectra (d) and near-field enhancement and surface current maps (e) of a GNR dimer in parallel tip-to-tip configuration at different separations (see labels). The inset shows detail of the 1 nm gap region. (f) Near-field intensity enhancement maps under left- and right-circularly polarized light irradiation for GNR dimers in perpendicular tip-to-tip configuration for a vertical offset of 10 nm. (g) Circular dichroism spectra under the same configuration as in (f) for offset distances of 0−10 nm. (h) Near-field enhancement maps under left- and right-circularly polarized light irradiation for GNRs arranged along a helix (110 nm radius and 110 nm pitch). (i) Circular dichroism of the same structure as in (h) for incidence along the helix axis (blue) and at 45° (green).

In all cases, smaller separation distances lead to higher field intensity enhancements, reaching values above 5×10^5. It should also be noted that in tip-to-valley configurations, the coupled mode yields extended hotspots that may be useful to achieve high SERS enhancement (and resulting signal) over large volumes. The occurrence of these extended hotspots can be explained by the larger areas of surfaces placed

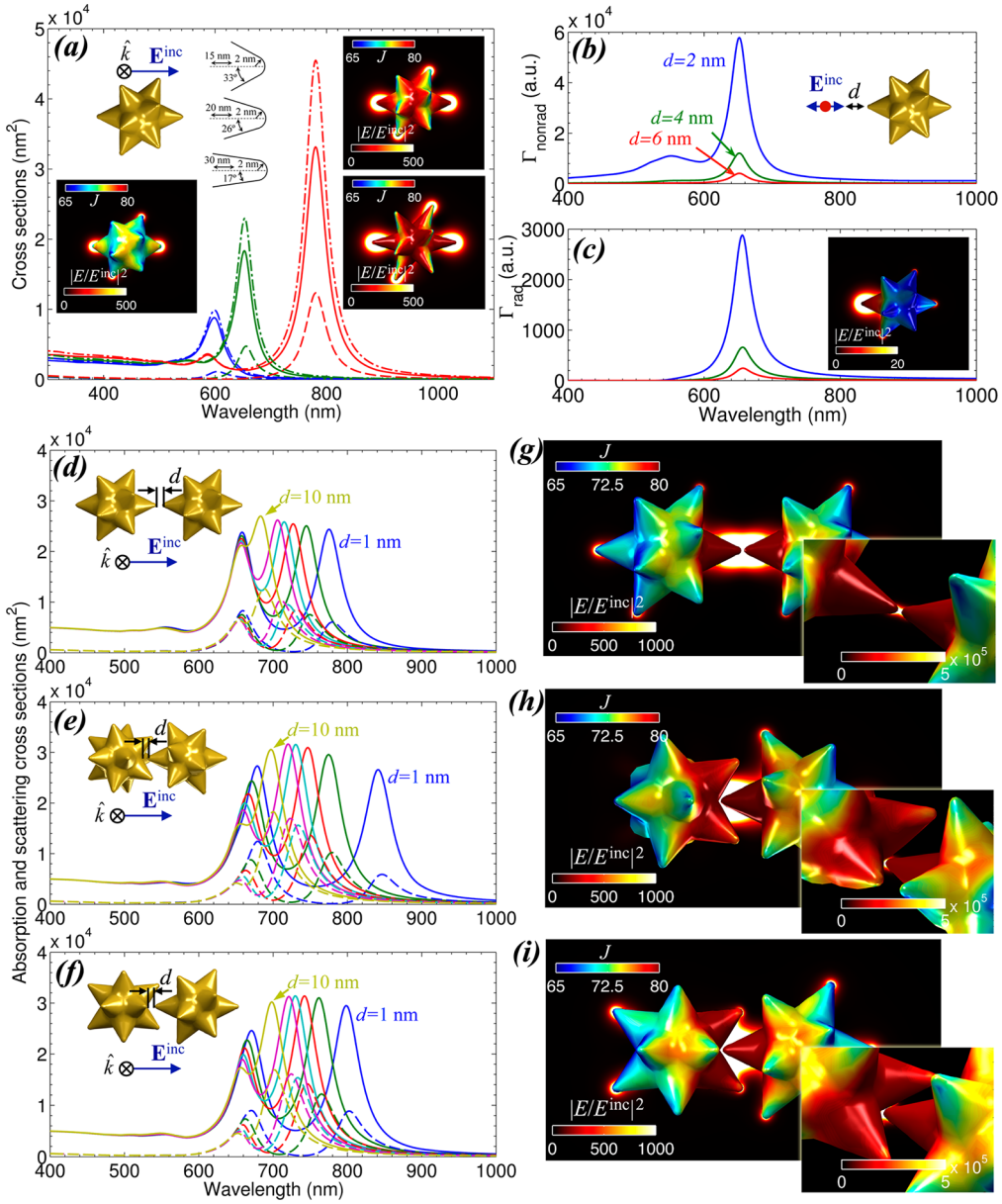

Figure 3. Modeling gold nanostars (GNSs). (a) Absorption (solid curves), scattering (dashed curves), and extinction (dash-dotted curves) of water-immersed GNSs (core diameter 18 nm) with 12 branches (tip apex 2 nm) of lengths 15 nm (blue), 20 nm (green, shown in inset), or 30 nm (red). The insets also show geometrical details for the three GNSs, along with maps of the surface electric current and electric near-field intensity enhancement along a plane perpendicular to the light incidence direction, calculated at the resonant wavelengths of 599, 653, and 780 nm. (b) Normalized nonradiative decay rate (Γ_{nonrad}) of a quantum dot placed at distances d = 2 nm (blue), d = 4 nm (green), and d = 6 nm (red) from one of the tips. The transition dipole is taken along the tip normal (see inset). (c) Same as (b), for the normalized radiative decay rate (Γ_{rad}). (d−f) Absorption (solid curves) and scattering (dashed curves) spectra for GNS dimers in tip-to-tip (d), tip-to-valley (e), and coplanar tip-to-valley (f) configurations for separations in the d = 1−10 nm range. (g−i) Surface electric current distribution and electric near-field enhancement of hybridized plasmons in tip-to-tip (g), tip-to-valley (h), and coplanar tip-to-valley (i) geometries for d = 1 nm. The field intensity enhancement reaches values >5 × 10^5 (see inset).

in close proximity. From the thumb rule of $\sim|E/E^{inc}|^4$ scaling of SERS intensity with electric field amplitude E, enhancement values above 10^{11} seem to be attainable in both tip-to-tip and tip-to valley configurations.

We now illustrate the interaction of a nanostar with a planar metal surface. This geometrical configuration has been successfully applied in actual experiments that report a controlled 10^{10} SERS enhancement from molecules that are sandwiched in the star−film gap.[35,51] We analyze this type of system in Figure 4. The underlying principle of the resulting enhancement is similar to the picture drawn from Figure 1. Interestingly, our simulations show large electric field enhancements when the nanostar is illuminated at an incidence angle of 45°, but only very poor enhancement is obtained under normal incidence, as excitation of the gap mode is forbidden by symmetry when a relatively uniform star is placed with

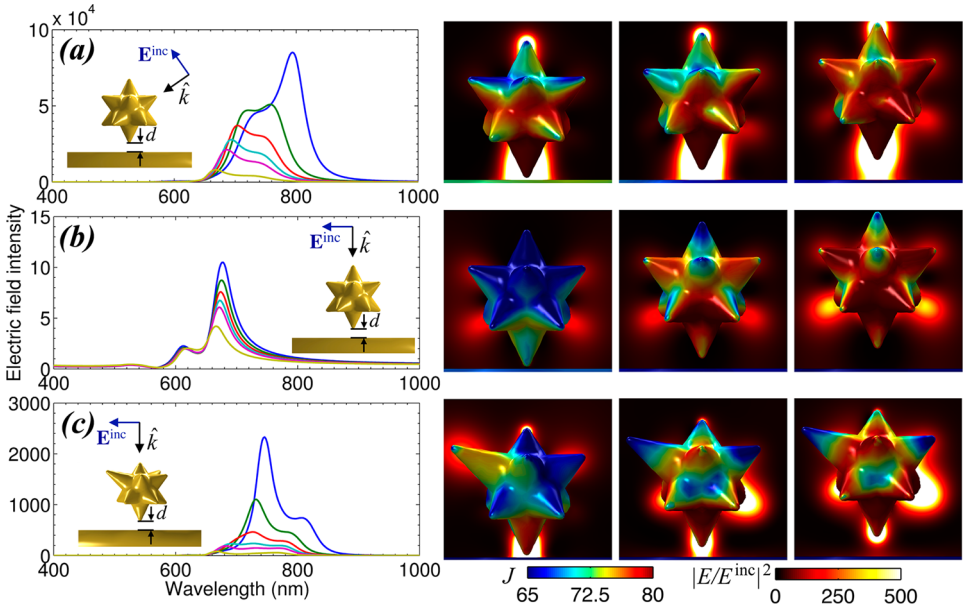

Figure 4. Close interactions between gold nanostars (GNSs) and a gold substrate. (a) Left: extinction spectra of a GNS placed at distances 1−10 nm from a planar gold film (surface-to-surface separation), under p-polarized (TM) irradiation at 45° incidence angle. Right: electric near-field intensity maps and surface electric current (dBμA/m) at the frequency of maximum extinction for separations of 1, 5, and 10 nm. (b) Same as (a) under normal light incidence. (c) Same as (b) for a slightly asymmetric star.

its tip oriented along the planar surface normal. A more asymmetric nanostar, such as those that are likely formed in actual experiments, immediately solves this problem and produces strong gap enhancement even under normal incidence illumination; this is illustrated in Figure 4 by simply elongating one of the tips of the nanostar.

Dense Nanoparticle Arrays. Perhaps an area in which the computational power of MLFMA is more clearly illustrated is in the simulation of dense assemblies of nanoparticles. Such nanoparticle arrays are commonly used for a vast range of applications, mostly based on empirical intuition, as their computation is highly demanding and it is usually reduced to capture only small subsystems or simplified versions of the structure. In a first example, we consider 1447 nanorods that are randomly packed inside a film-like $1 \times 1 \times 0.2$ μm^3 box with a minimum distance between particles surfaces of 1 nm (see Figure 5a,b). The calculated absorption and scattering spectra display significant broadening (Figure 5b), which is a typical signature of systems composed of multiple plasmon couplings, with random local arrangements and mode shifts.

Our calculations enable us to examine not only scattering and absorption spectra but also the efficiency of these films as SERS substrates. Enhancement maps are shown in Figure 5 for the near electric field intensity $|\mathbf{E}_{in}|^2$ at an incidence wavelength λ_{in} = 785 nm (normalized to the incident intensity), the emission/collected intensity $|\mathbf{E}_{out}|^2$ radiated by an excited molecule at a wavelength λ_{out} = 879.98 nm (Raman shift of 1375 cm^{-1}) as a function of its position in the sample (normalized to the emission in the absence of the particle), and the SERS intensity, which is simply given by the product $|\mathbf{E}_{in}|^2 \cdot |\mathbf{E}_{out}|^2$. These calculations illustrate the evolution of hotspots when moving from the incident wavelength to the emission wavelength, which we attribute to the strong dependence of the resonant gap plasmons on the local rod arrangement. Strong SERS emission is favored at positions in which a compromise between hotspots at both wavelengths is reached (see Figure 5f,i). Incidentally, the SERS maps calculated at different heights across the film (Figure 5c−g) clearly show the decay in enhancement efficiency as we move deeper inside the film (see SI movie S1).

A different picture can be drawn when crystalline order is imposed on the nanorod assembly. In particular, recent experimental work has demonstrated the feasibility of obtaining supercrystals of gold nanorods oriented perpendicularly with respect to a substrate, leading to a multilayer hexagonal arrangement.[52] It has also been reported that such supercrystals may display antenna effects, leading to additional electric near-field enhancements, which was claimed to enable ultrasensitive detection of scrambled prions.[53] We show in Figure 6 that such an arrangement can readily be modeled using MLFMA. We consider nine layers containing a total of 895 nanorods. Simulations were carried out for illumination at normal incidence (parallel to the nanorods axis) and linear polarization in the plane of the substrate. The calculated spectra (Figure 6b) display a rich behavior with at least four well-defined

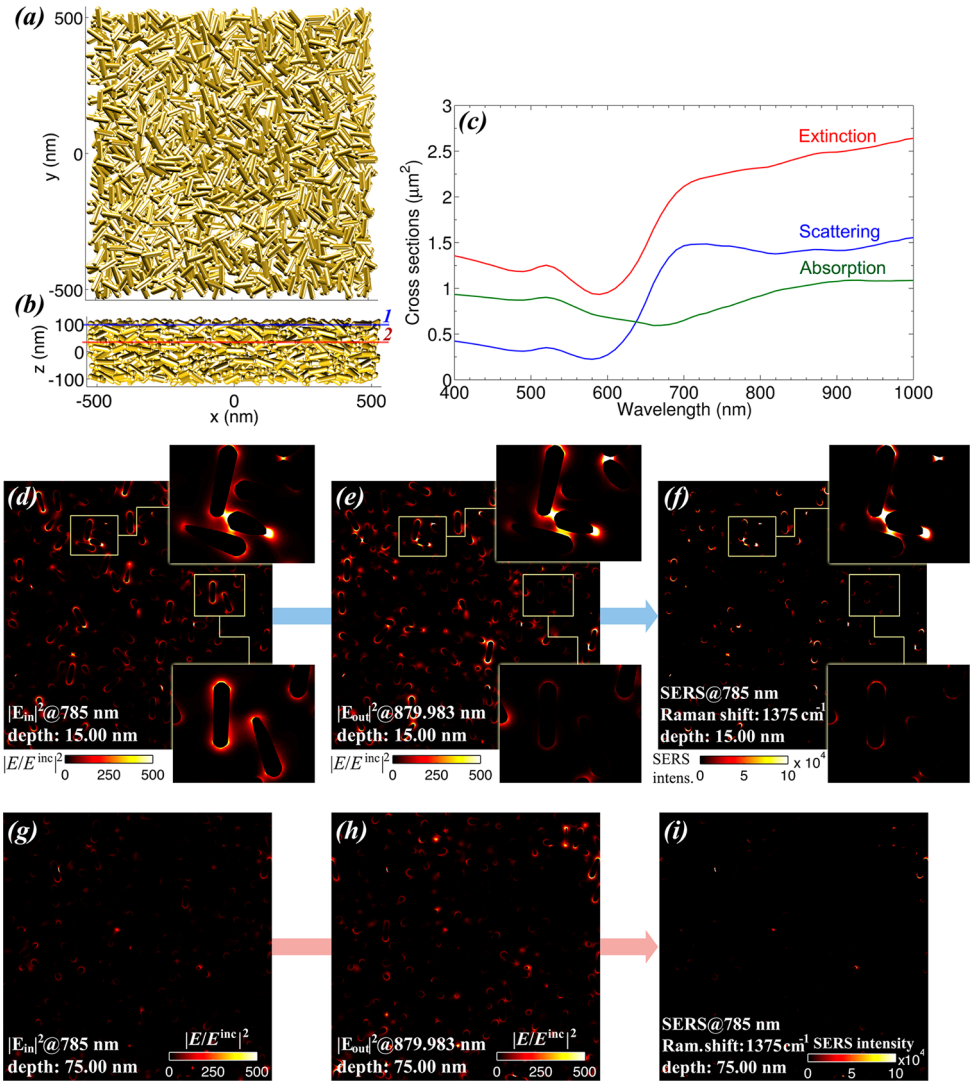

Figure 5. Plasmonic and surface-enhanced Raman scattering performance of highly complex disordered structures, simulated with M³. Top view (a) and side view (b) of an in-water colloidal deposition of 1447 gold nanorods (80 × 21 nm² size, octagonal cross section; see Figure 2) compacted in a 1 × 1 × 0.2 μm³ box (minimum surface-to-surface separation is 1 nm). (c) Scattering (blue), absorption (green), and extinction (red) cross sections for light incidence as shown in the inset. (d,e) Electric near-field intensity enhancements showing the emergence and disappearance of hotspots as we move between two different wavelengths. The plane of representation is indicated in blue (1) in (b). (f) Distribution of SERS enhancement for illumination at the wavelength of (d) and emission at the wavelength of (e) (Raman shift of 1375 cm^{-1}). (g–i) Same as (d–f) for a deeper plane (labeled (2), red, in (b)).

scattering bands but only two well-defined absorption maxima. This is in stark contrast to the spectra for disordered nanorods (Figure 5c). As the rod spacing is small compared with the illumination wavelengths, photonic crystal effects can be ruled out; instead, the observed spectral features seem to originate in the metamaterial response of the periodic arrangement of relatively small nanorods, which is expected to sustain well-defined propagation modes. These modes form standing waves due to spatial confinement within the finite box in which the structure is contained. Inspection of the near-field plots in Figure 6 reveals clear standing-wave patterns, which produce relatively high SERS enhancement over large regions of the material, thus indicating the suitability of these types of structures to sample large volumes. A movie showing the changes in hotspot distribution as we move deeper inside the crystal is provided as Supporting Information (movie S2), where we observe the presence of hotspots in regions corresponding to maxima of the noted standing waves, which are distributed over the sample at different resonant depths. This is in contrast to the disordered structure of Figure 5, where no transmission bands are allowed, as illustrated by an analogous movie (SI movie S1), revealing instead a gradual depletion of hotspots when moving toward deeper regions.

CONCLUSIONS

After several decades of impressive advancements in the fundamental understanding and practical

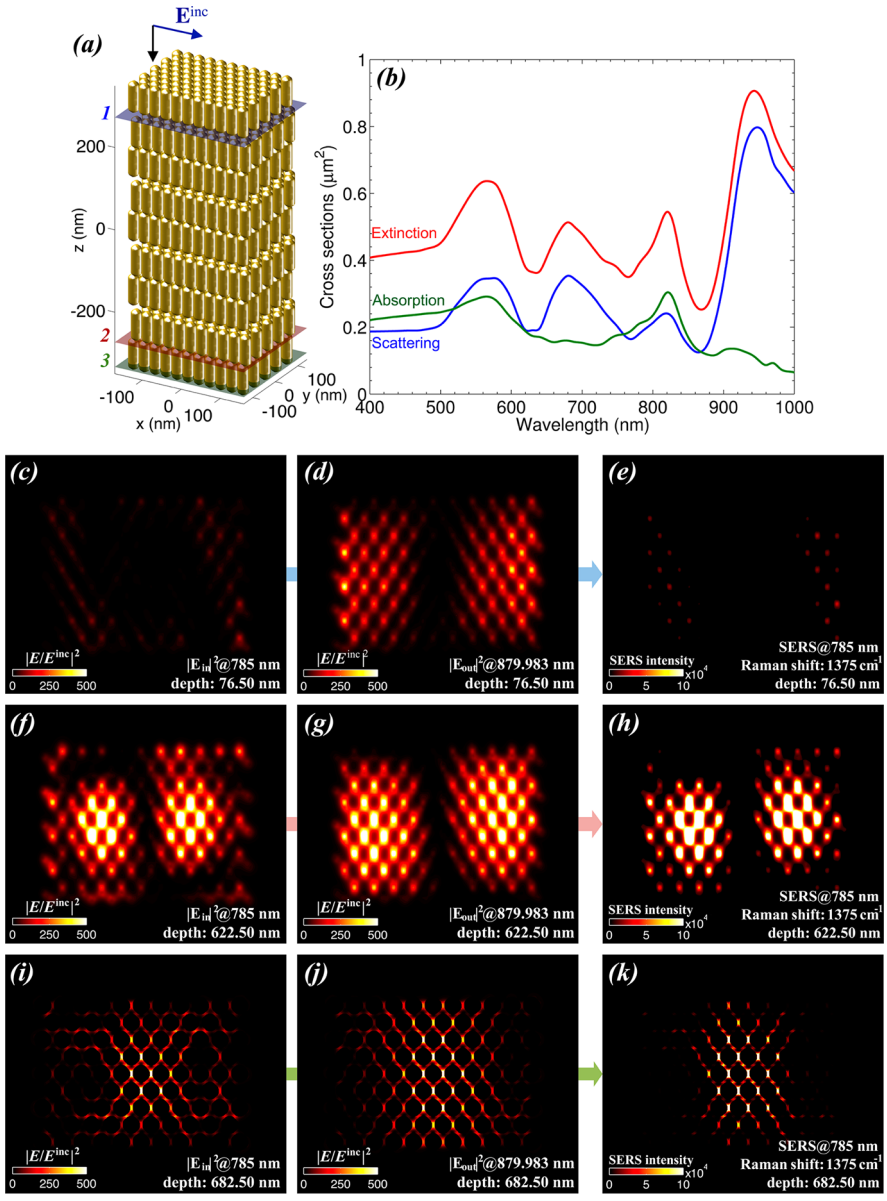

Figure 6. Response and surface-enhanced Raman scattering performance of a three-dimensional plasmonic crystal, simulated with M³. Same as Figure 5, for a plasmonic crystal composed of 895 airborne nanorods (75 × 25 nm² in size, asymmetric octagonal section; see Figure 2) stacked in nine layers with hexagonal intralayer arrangement (see (a), surface-to-surface separation is 3 nm along and across layers). The near-field and SERS maps of (c−e) are represented over the blue sheet of (a), whereas the maps of (f−h) correspond to the red sheet of (a) and (i−k) to the green sheet. The SERS maps (e,h,k) are constructed from the near-fields to their left following the same procedure as in Figure 5.

application of plasmonics, the need for better electromagnetic simulation tools becomes apparent. By and large, published simulations have either a fundamental character, concentrating on relatively simple structures, or a qualitative purpose. Oftentimes, commercial software is used to deal with complex structures, which are still limited by the widespread use of volumetric methods (FDTD, DDA, FEMs, *etc.*). In an effort to extend the validity of these approaches to larger structures, volumetric codes generally involve a large number of convergence parameters (*e.g.*, in the use of absorbing boundary conditions), thus producing not fully reproducible results that are sometimes plagued with errors and instabilities.

The present work illustrates that surface integral equation methods, combined with advanced method-of-moments parametrizations (here abbreviated SIE-MoM) and expedited *via* MLFMA, offer a viable alternative to cope with large complex structures and have clear advantages such as their reduced computational demand, both in time and memory, their robustness against sharp dielectric contrasts, and their small number of critical parameters (essentially the discretization size and the number of boundary elements). Although boundary parametrization represents a challenge compared with volume discretization, SIE methods might be

the only viable approach to the predictive simulation of large systems such as those involved in the realistic engineering of nanoplasmonic devices and sensing nanostructures.

Conflict of Interest: The authors declare no competing financial interest.

Acknowledgment. D.M.S., J.M.T., and F.O. acknowledge funding from the European Regional Development Fund (ERDF) and the Spanish Government, Ministerio de Economía y Competitividad, Dirección General de Investigación Científica y Técnica (TEC2011-28784-C02-01, TEC2011-28784-C02-02, CONSOLIDERINGENIO 2010 CSD2008-00068, project TACTICA), from the ERDF and the Galician Regional Government under Projects CN2012/279 and CN2012/260 (AtlantTIC), and the Plan I2C (2011-2015), and from the ERDF and the Extremadura Regional Government (IB13185). L.M.L.-M. acknowledges funding from the European Research Council (ERC Advanced Grant #267867 Plasmaquo). F.J.G.A. acknowledges funding from the European Commission (Graphene Flagship CNECT-ICT-604391 and FP7-ICT-2013-613024-GRASP).

Supporting Information Available: Full description of the calculation method, computing times, and movies of SERS enhancement in nanorod films. This material is available free of charge *via* the Internet at http://pubs.acs.org.

REFERENCES AND NOTES

1. Polman, A. Plasmonics Applied. *Science* **2008**, *322*, 868–869.
2. Stockman, M. I. Nanoplasmonics: Past, Present, and Glimpse into Future. *Opt. Express* **2011**, *19*, 22029–22106.
3. O'Neal, D. P.; Hirsch, L. R.; Halas, N. J.; Payne, J. D.; West, J. L. Photo-thermal Tumor Ablation in Mice Using Near Infrared-Absorbing Nanoparticles. *Cancer Lett.* **2004**, *209*, 171–176.
4. Zia, R.; Schuller, J. A.; Chandran, A.; Brongersma, M. L. Plasmonics: The Next Chip-Scale Technology. *Mater. Today* **2006**, *9*, 20–27.
5. Oulton, R. F.; Sorger, V. J.; Zentgraf, T.; Ma, R. M.; Gladden, C.; Dai, L.; Bartal, G.; Zhang, X. Plasmon Lasers at Deep Subwavelength Scale. *Nature* **2009**, *461*, 629–632.
6. Atwater, H. A.; Polman, A. Plasmonics for Improved Photovoltaic Devices. *Nat. Mater.* **2010**, *9*, 205–213.
7. Noginov, M. A.; Zhu, G.; Belgrave, A. M.; Bakker, R.; Shalaev, V. M.; Narimanov, E. E.; Stout, S.; Herz, E.; Suteewong, T.; Wiesner, U. Demonstration of a Spaser-Based Nanolaser. *Nature* **2009**, *460*, 1110–1113.
8. Akimov, A. V.; Mukherjee, A.; Yu, C. L.; Chang, D. E.; Zibrov, A. S.; Hemmer, P. R.; Park, H.; Lukin, M. D. Generation of Single Optical Plasmons in Metallic Nanowires Coupled to Quantum Dots. *Nature* **2007**, *450*, 402–406.
9. Fakonas, J. S.; Lee, H.; Kelaita, Y. A.; Atwater, H. A. Two-Plasmon Quantum Interference. *Nat. Photonics* **2014**, *8*, 317–320.
10. García de Abajo, F. J. Optical Excitations in Electron Microscopy. *Rev. Mod. Phys.* **2010**, *82*, 209–275.
11. Berini, P. Plasmon-Polariton Waves Guided by Thin Lossy Metal Films of Finite Width: Bound Modes of Symmetric Structures. *Phys. Rev. B* **2000**, *61*, 10484–10503.
12. García de Abajo, F. J. Nonlocal Effects in the Plasmons of Strongly Interacting Nanoparticles, Dimers, and Waveguides. *J. Phys. Chem. C* **2008**, *112*, 17983–17987.
13. Esteban, R.; Borisov, A. G.; Nordlander, P.; Aizpurua, J. Bridging Quantum and Classical Plasmonics with a Quantum-Corrected Model. *Nat. Commun.* **2012**, *3*, 825.
14. Ashcroft, N. W.; Mermin, N. D. *Solid State Physics*; Harcourt College Publishers: New York, 1976.
15. Myroshnychenko, V.; Rodríguez-Fernández, J.; Pastoriza-Santos, I.; Funston, A. M.; Novo, C.; Mulvaney, P.; Liz-Marzán, L. M.; García de Abajo, F. J. Modelling the Optical Response of Gold Nanoparticles. *Chem. Soc. Rev.* **2008**, *37*, 1792–1805.
16. Ouyang, F.; Isaacson, M. Surface Plasmon Excitation of Objects with Arbitrary Shape and Dielectric Constant. *Philos. Mag. B* **1989**, *60*, 481–492.
17. Mie, G. Beiträge zur Optik trüber Medien, speziell kolloidaler Metallösungen. *Ann. Phys. (Leipzig, Ger.)* **1908**, *25*, 377–445.
18. Draine, B. T. The Discrete-Dipole Approximation and Its Application to Interstellar Graphite Grains. *Astrophys. J.* **1988**, *333*, 848–872.
19. Hao, F.; Nehl, C. L.; Hafner, J. H.; Nordlander, P. Plasmon Resonances of a Gold Nanostar. *Nano Lett.* **2007**, *7*, 729–732.
20. Jin, J. *The Finite Element Method in Electromagnetics*; Wiley: New York, 2002.
21. Zhang, S.; Bao, K.; Halas, N. J.; Xu, H.; Nordlander, P. Substrate-Induced Fano Resonances of a Plasmonic Nanocube: A Route to Increased-Sensitivity Localized Surface Plasmon Resonance Sensors Revealed. *Nano Lett.* **2011**, *11*, 1657–1663.
22. Harrington, R. F. *Field Computation by Moment Method*; IEEE Press: New York, 1993.
23. Taboada, J. M.; Rivero, J.; Obelleiro, F.; Araújo, M. G.; Landesa, L. Method-of-Moments Formulation for the Analysis of Plasmonic Nanooptical Antennas. *J. Opt. Soc. Am. A* **2011**, *28*, 1341–1348.
24. Nelayah, J.; Kociak, M.; Stéphan, O.; García de Abajo, F. J.; Tencé, M.; Henrard, L.; Taverna, D.; Pastoriza-Santos, I.; Liz-Marzán, L. M.; Colliex, C. Mapping Surface Plasmons on a Single Metallic Nanoparticle. *Nat. Phys.* **2007**, *3*, 348–353.
25. Yamamoto, N.; Araya, K.; García de Abajo, F. J. Photon Emission from Silver Particles Induced by a High-Energy Electron Beam. *Phys. Rev. B* **2001**, *64*, 205419.
26. Song, J. M.; Lu, C. C.; Chew, W. C. Multilevel Fast Multipole Algorithm for Electromagnetic Scattering by Large Complex Objects. *IEEE Trans. Antennas Propag.* **1997**, *45*, 1488–1493.
27. Taboada, J. M.; Araújo, M. G.; Obelleiro, F.; Rodríguez, J. L.; Landesa, L. MLFMA-FFT Parallel Algorithm for the Solution of Extremely Large Problems in Electromagnetics. *Proc. IEEE* **2013**, *101*, 350–363.
28. Araújo, M. G.; Solís, D. M.; Rivero, J.; Taboada, J. M.; Obelleiro, F. Solution of Large-Scale Plasmonic Problems with the Multilevel Fast Multipole Algorithm. *Opt. Lett.* **2012**, *37*, 416–418.
29. Solís, D. M.; Taboada, J. M.; Araújo, M. G.; Obelleiro, F.; Rubiños-López, J. O. Design of Optical Wide-Band Log-Periodic Nanoantennas Using Surface Integral Equation Techniques. *Opt. Commun.* **2013**, *301–302*, 61–66.
30. Obelleiro, F.; Taboada, J. M.; Solís, D. M.; Bote, L. Directive Antenna Nanocoupler to Plasmonic Gap Waveguides. *Opt. Lett.* **2013**, *38*, 1630–1632.
31. Solís, D. M.; Taboada, J. M.; Obelleiro, F.; Landesa, L. Optimization of an Optical Wireless Nanolink Using Directive Nanoantennas. *Opt. Express* **2013**, *21*, 2369–2377.
32. Thongrattanasiri, S.; García de Abajo, F. J. Optical Field Enhancement by Strong Plasmon Interaction in Graphene Nanostructures. *Phys. Rev. Lett.* **2013**, *110*, 187401.
33. Johnson, P. B.; Christy, R. W. Optical Constants of the Noble Metals. *Phys. Rev. B* **1972**, *6*, 4370–4379.
34. Romero, I.; Aizpurua, J.; Bryant, G. W.; García de Abajo, F. J. Plasmons in Nearly Touching Metallic Nanoparticles: Singular Response in the Limit of Touching Dimers. *Opt. Express* **2006**, *14*, 9988–9999.
35. Rodríguez-Lorenzo, L.; Alvarez-Puebla, R. A.; Pastoriza-Santos, I.; Mazzucco, S.; Stéphan, O.; Kociak, M.; Liz-Marzán, L. M.; García de Abajo, F. J. Zeptomol Detection through Controlled Ultrasensitive Surface-Enhanced Raman Scattering. *J. Am. Chem. Soc.* **2009**, *131*, 4616–4618.
36. García de Abajo, F. J.; Aizpurua, J. Numerical Simulation of Electron Energy Loss near Inhomogeneous Dielectric. *Phys. Rev. B* **1997**, *56*, 15873.
37. Love, A. E. H. The Integration of Equations of Propagation of Electric Waves. *Philos. Trans. R. Soc. London, Ser. A* **1901**, *197*, 1–45.
38. Stratton, J. A.; Chu, L. J. Diffraction Theory of Electromagnetic Waves. *Phys. Rev.* **1939**, *56*, 99–107.
39. Stratton, J. A. *Electromagnetic Theory*; McGraw-Hill: New York, 1941.

40. Coifman, R.; Rokhlin, V.; Wanzura, S. The Fast Multipole Method for the Wave Equation: A Pedestrian Prescription. *IEEE Antennas Propag. Mag.* **1993**, *35*, 7–12.
41. Pérez-Juste, J.; Pastoriza-Santos, I.; Liz-Marzán, L. M.; Mulvaney, P. Gold Nanorods: Synthesis, Characterization and Applications. *Coord. Chem. Rev.* **2005**, *249*, 1870–1901.
42. Goris, B.; Bals, S.; Van den Broek, W.; Carbó-Argibay, E.; Gómez-Graña, S.; Liz-Marzán, L. M.; Van Tendeloo, G. Atomic Scale Determination of Surface Facets in Gold Nanorods. *Nat. Mater.* **2012**, *11*, 930–935.
43. Scarabelli, L.; Grzelczak, M.; Liz-Marzán, L. M. Tuning Gold Nanorod Synthesis through Pre-reduction with Salicylic Acid. *Chem. Mater.* **2013**, *25*, 4232–4238.
44. Novotny, L. Effective Wavelength Scaling for Optical Antennas. *Phys. Rev. Lett.* **2007**, *98*, 266802.
45. Guerrero-Martínez, A.; Alonso-Gómez, J. L.; Auguié, B.; Cid, M. M.; Liz-Marzán, L. M. From Individual to Collective Chirality in Metal Nanoparticles. *Nano Today* **2011**, *6*, 381–400.
46. Ben-Moshe, A.; Maoz, B. M.; Govorov, A. O.; Markovich, G. Chirality and Chiroptical Effects in Inorganic Nanocrystal Systems with Plasmon and Exciton Resonances. *Chem. Soc. Rev.* **2013**, *42*, 7028–7041.
47. Guerrero-Martínez, A.; Auguié, B.; Alonso-Gómez, J. L.; Džolić, Z.; Gómez-Graña, S.; Žinić, M.; Cid, M. M.; Liz-Marzán, L. M. Intense Optical Activity *via* 3D Chiral Ordering of Plasmonic Nanoantennas. *Angew. Chem., Int. Ed.* **2011**, *50*, 5499–5503.
48. Guerrero-Martínez, A.; Barbosa, S.; Pastoriza-Santos, I.; Liz-Marzán, L. M. Nanostars Shine Bright for You. Colloidal Synthesis, Properties and Applications of Branched Metallic Nanoparticles. *Curr. Opin. Colloid Interface Sci.* **2011**, *16*, 118–127.
49. Yuan, H.; Fales, A. M.; Vo-Dinh, T. TAT Peptide-Functionalized Gold Nanostars: Enhanced Intracellular Delivery and Efficient NIR Photothermal Therapy Using Ultralow Irradiance. *J. Am. Chem. Soc.* **2012**, *134*, 11358–11361.
50. Blanco, L. A.; García de Abajo, F. J. Spontaneous Light Emission in Complex Nanostructures. *Phys. Rev. B* **2004**, *69*, 205414.
51. Alvarez-Puebla, R.; Liz-Marzán, L. M.; García de Abajo, F. J. Light Concentration at the Nanometer Scale. *J. Phys. Chem. Lett.* **2010**, *1*, 2428–2434.
52. Guerrero-Martínez, A.; Pérez-Juste, J.; Carbó-Argibay, E.; Tardajos, G.; Liz-Marzán, L. M. Gemini Surfactant-Directed Self-Assembly of Monodisperse Gold Nanorods into Standing Superlattices. *Angew. Chem., Int. Ed.* **2009**, *48*, 9484–9488.
53. Alvarez-Puebla, R. A.; Agarwal, A.; Manna, P.; Khanal, B. P.; Aldeanueva-Potel, P.; Carbó-Argibay, E.; Pazos-Pérez, N.; Vigderman, L.; Zubarev, E. R.; Kotov, N. A.; Liz-Marzán, L. M. Gold Nanorods 3D-Supercrystals as SERS Substrates for the Rapid Detection of Scrambled Prions. *Proc. Natl. Acad. Sci. U.S.A.* **2011**, *108*, 8157–8161.